Juri Barthel, 1, \* Paul M. Zeiger, 2 Ján Rusz, 2 and Leslie J. Allen 3

<sup>1</sup>Ernst Ruska-Centre (ER-C 2) Forschungszentrum Juelich GmbH, 52425 Juelich, Germany <sup>2</sup>Department of Physics and Astronomy, Uppsala University, P.O. Box 516, 75120 Uppsala, Sweden <sup>3</sup>School of Physics, University of Melbourne, Parkville, VIC 3010, Australia (Dated: March 13, 2024)

We propose a simple approach to simulating the phonon sector in electron energy-loss spectroscopy (EELS), as implemented in scanning transmission electron microscopy. Simplification of the problem is obtained by working with the phonon density of states, a function of phonon energy, which is an integral over the details of the dispersion relations due to the correlated motions of the atoms. For a given phonon density of states we derive a spectral distribution function, to distribute the total inelastic scattering, as calculated within the quantum excitation of phonons model, into an energy-loss/gain spectrum. The spectral distribution is obtained assuming a linear relationship between inelastic phonon scattering and atomic mean-squared displacements, a good approximation for phonon EELS with a detector covering only moderate scattering angles. We provide examples of the usefulness of the proposed approach in the modeling and interpretation of experimental phonon EELS data.

#### I. INTRODUCTION

The development of monochromated sources in tandem with aberration correction has made it possible to probe the vibrational states of a material at the atomic scale using the electron energy-loss spectroscopy (EELS) mode available in scanning transmission electron microscopy (STEM) [1]. Subsequently, a number of experiments have been carried out, mainly on thinner samples containing light elements, for example Refs. [2–11]. Thicker specimens containing heavier elements have also been examined using STEM phonon EELS, for example Refs. [12–14] and we will make comparisons with experimental results in the first two of these papers. A variety of approaches have been used to model and understand the physics associated with the experimental results [2, 8, 10, 15–26]. The relationship between some of these approaches has recently been explored in a paper by the present authors [27] and the importance of being able to correctly account for the channeling (multiple elastic scattering of the probing electrons), particularly in the case of thicker specimens, was emphasized.

In this paper we propose a simple approach to simulate energy-loss/gain spectra in the phonon sector of STEM EELS. We propose to derive a spectral distribution function (SDF) for a given phonon density of states (PDOS) by assuming proportionality between the strength of inelastic scattering and atomic mean-squared displacements. The assumption of proportionality is certainly satisfied for single-phonon excitations near a temperature of absolute zero and at smaller scattering angles as the temperature increases. We will see that it remains a reasonable assumption at room temperature and, even in that case, for off-axis detectors encompassing not too large scattering angles. However, since the

The PDOS, arising due to correlated vibrational modes, is a function of phonon energy. To take into account a specimen at non-zero temperature, Boltzmann factors are used to separate the contributions to the energy-loss and the energy-gain sectors of the SDF, assuming dominance of single-phonon excitations. The SDF can then be scaled, using the total phonon scattering calculated in the quantum excitation of phonons (QEP) model [18], into an energy-loss/gain spectrum. The QEP model takes into account, in a global way and to a good approximation, the effects of channeling of the probe as a function of probe position and sample thickness. In its conventional form, the QEP model integrates all possible phonon excitations from a given set of initial states without providing any energy-resolved information, whereas here we distribute the inelastic phonon scattering into an energy-loss/gain spectrum.

The main advantage of the simple approach is the speed of calculation, which is of the order of seconds. We demonstrate its utility by application to recently published experimental data, an improvement on simply comparing EELS data to a PDOS.

# II. EINSTEIN MODEL AND MEAN-SQUARE DISPLACEMENT

It will suffice here to consider phonon excitation in an Einstein model. We assume that the atoms vibrate independently in an isotropic potential for an harmonic oscillator. The atomic wave function for the nuclear subsystem factorizes into a product of wave functions for three orthogonal directions, each of which has the form of a standard harmonic oscillator wave function, as

$$\Psi_{\mathbf{n}}(\mathbf{u}) = \Psi_{n_1}(u_1) \,\Psi_{n_2}(u_2) \,\Psi_{n_3}(u_3) \,, \tag{1}$$

PDOS integrates over momentum transfer, the approach discussed here is suitable for energy-loss detectors covering an angular range of at least one Brillouin zone, a common scenario in phonon EELS mapping.

<sup>\*</sup> ju.barthel@fz-juelich.de

where  $\mathbf{u}$ , with Cartesian components  $(u_1, u_2, u_3)$ , denotes the displacement of the atom from its equilibrium position. The oscillator wave function for a spatial dimension is identified by an index  $i \in \{1, 2, 3\}$ . Generalizing Eq. (F2) in Ref. [17], the transition potential in reciprocal space for a transition from an initial state with quantum numbers  $\mathbf{m} = (m_1, m_2, m_3)$  to a final state with quantum numbers  $\mathbf{n} = (n_1, n_2, n_3)$  can be written as

$$H_{\mathbf{nm}}(\mathbf{q}) = \frac{h^2}{2\pi m} f_e(q) e^{-2\pi i \mathbf{q} \cdot \mathbf{R}} \times \prod_i \langle \Psi_{n_i}(u_i) | e^{-2\pi i q_i u_i} | \Psi_{m_i}(u_i) \rangle . \quad (2)$$

Here m is the relativistically corrected mass of the probing electron and  $f_{\rm e}(q)$  is an electron scattering factor for the atom, depending on the magnitude q of the scattering vector  $\mathbf{q}$ , and which is located at position  $\mathbf{R}$ .

In the specific case of excitations from the ground state  $\mathbf{0} = (0,0,0)$  to the state  $\mathbf{n} = (n_1,n_2,n_3)$ , for example, it can be shown that Eq. (2) becomes [17]

$$H_{\mathbf{n0}}(\mathbf{q}) = \frac{h^2}{2\pi m} f_{\mathbf{e}}(q) e^{-2\pi i \mathbf{q} \cdot \mathbf{R}} \times \prod_{i} \frac{\left(-i\sqrt{2\frac{M}{m_a}q_i^2}\right)^{n_i}}{\sqrt{n_i!}} e^{-\frac{M}{m_a}q_i^2} , \quad (3)$$

where  $m_a$  is the mass of the atom,  $M/m_a \equiv 2\pi^2 \langle u_0^2 \rangle$  and  $\langle u_0^2 \rangle$  is the mean-square displacement (MSD) of the harmonic oscillator for the ground state.

There are three possibilities for single-phonon excitation, i.e., each of the  $n_i = 1$  in turn whilst the remaining quantum numbers remain zero. Incoherently summing these three possibilities, the integrated inelastic scattered intensity for a plane incident wave into a detector D is given by

$$I_{\text{inel}}^{D} \equiv \sum_{\mathbf{n}} \int_{D} |H_{\mathbf{n0}}(\mathbf{q})|^{2} d\mathbf{q}$$

$$= \frac{h^{4}}{m^{2}} \left[ \int_{D} f_{e}^{2}(q) q^{2} e^{-4\pi^{2} \langle u_{0}^{2} \rangle q^{2}} d\mathbf{q} \right] \langle u_{0}^{2} \rangle , \quad (4)$$

where we have used  $q^2 = \sum_i q_i^2$  and the integral in square brackets is determined by the detector. Assuming a sufficiently small product  $\langle u_0^2 \rangle q^2$  within the detector area, the important point to note is that the inelastic scattering intensity is approximately proportional to the MSD  $\langle u_0^2 \rangle$ . We note that single-phonon de-excitations  $H_{0n}(\mathbf{q})$  could also be considered but would not change the form of Eq. (4), tacitly assuming T>0 K. This result was derived at absolute zero of temperature but remains a good approximation at room temperature, despite single-phonon excitations involving initial states having quantum numbers larger than one also then playing a role. In that case, the respective transition probabilities include, in addition, higher-order terms of the product  $\langle u_0^2 \rangle q^2$  (see

Appendix E in Ref. [27]) via generalized Laguerre polynomials, which suggest a deviation from the linear relation. However, calculations of inelastic scattering due to phonon excitation at room temperature in the QEP model [18] (also see Appendix A), show that the inelastically scattered intensity  $I_{\text{inel}}^D$  increases approximately linearly with increasing mean-squared displacement (MSD) of the atoms [20, 27]. An example is given in Fig. 1 for a thin silicon crystal in [110] orientation, under predominantly single-scattering conditions. The almost linear relationship between the strength of inelastic scattering and the MSD of the atoms is maintained, at least for the range of scattering angles considered, and is used in what follows to derive an approximate but simple way of calculating phonon electron energy-loss spectra for a given phonon density of states.

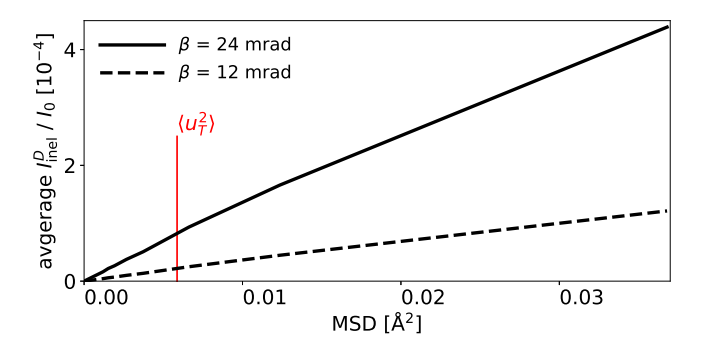


FIG. 1. Average fractional intensity of inelastic scattering  $I_{\rm inel}^D/I_0$ , where  $I_0$  is the intensity of the incident probe, as a function of the MSD of the atoms in the specimen. The average fractional intensity is calculated in the QEP model by scanning a 60-keV electron probe, with 28 mrad semiconvergence angle, across a unit cell of Si in [110] orientation. On-axis, circular detectors with collection semi angles  $\beta$  of 24 mrad (solid curve) and 12 mrad (dashed curve) were assumed. The vertical line marks the MSD of Si at a temperature of 300 K.

# III. PHONON DENSITY OF STATES AND SPECTRAL DISTRIBUTION FUNCTION

The MSD of an atom at a temperature T may be expressed as follows [28, 29]:

$$\langle u_T^2 \rangle = \frac{\hbar^2}{2m_a} \int_0^{E_m} \coth\left(\frac{E}{2k_B T}\right) \frac{g(E)}{E} dE .$$
 (5)

Here  $m_a$  is the mass of the atom,  $E_m$  is the maximum of the phonon energy E,  $k_{\rm B}$  is the usual Boltzmann constant and g(E) is the phonon density of states, normalized to one, and understood, in what follows, to always be at the temperature T. The phonon density of states g(E) may be measured by inelastic neutron scattering [28]. The numerical integration in Eq. (5) then gives the weighted average MSD  $\langle u_T^2 \rangle$  at a given temperature. The MSD is an exponent in the well-known Debye-Waller or temperature factor  $\exp(-2\pi^2\langle u_T^2\rangle q^2)$  and a key parameter in a conventional QEP calculation, which usually does not provide any energy-resolved detail.

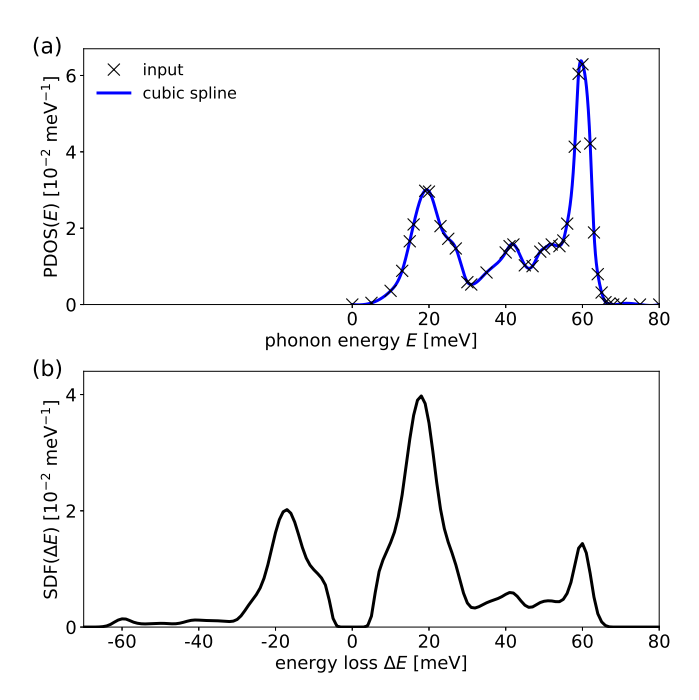


FIG. 2. (a) PDOS for Si with values digitized from the 300-K result in Fig. 1 of Kim  $et\ al.$  [30] (crosses) and interpolated with a cubic spline (blue curve). (b) Normalized spectral distribution function as derived from the PDOS in (a) at a temperature of 300 K.

As an example, consider the PDOS for a silicon crystal at T=300 K measured using inelastic neutron scattering by Kim et~al.~[30] - see Fig. 1 in that paper. We have digitized their result at the points shown by crosses in Fig. 2(a). These points were then interpolated by a cubic spline. Using Eq. (5) with the Si PDOS yields  $\langle u_T^2 \rangle = 0.00574$  Ų, as marked by a vertical line in Fig. 1, and this is close to a recommended experimental value at room temperature of 0.00572 Ų from the compilation in Ref. [31].

It is clear from Eq. (5) that the PDOS g(E) does not directly determine  $\langle u_T^2 \rangle$  at the temperature T but that the pertinent weighting at each phonon energy E in the interval  $[0, E_m]$  is

$$\langle u_{T,E}^2 \rangle = \frac{\hbar^2}{2m_a} \coth\left(\frac{E}{2k_{\rm B}T}\right) \frac{1}{E} ,$$
 (6)

where  $\langle u_{T,E}^2 \rangle$  is the MSD for an harmonic oscillator at temperature T and with frequency  $\omega = E/\hbar$ . This means that, assuming proportionality between the strength of inelastic scattering and the MSD, as derived for absolute zero in Eq. (4) and shown by example to be a good

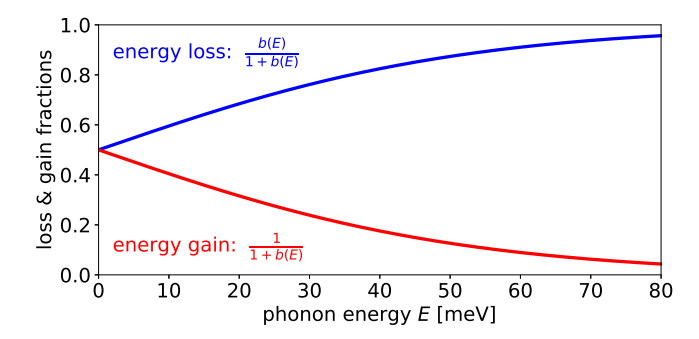


FIG. 3. Energy loss (upper blue curve) and energy gain (lower red curve) fractions for single-phonon excitations over the phonon energy range covered by the Si PDOS and at a temperature of  $300~\rm K.$ 

approximation at room temperature in Fig. 1, we have

$$I_{\rm inel}^D \approx C^D \langle u_T^2 \rangle = C^D \int_0^{E_m} g(E) \langle u_{T,E}^2 \rangle dE \ .$$
 (7)

The constant  $C^D$  is determined by carrying out a calculation for  $I_{\text{inel}}(\mathbf{q})$  in the QEP model [see Appendix A, Eq. (A3) for the detector geometry (c.f. the term in square brackets in Eq. (4)), which provides  $I_{\text{inel}}^D$  and hence an inelastically scattered fraction of the incident probe current  $I_0$  as  $I_{\text{inel}}^{D}/I_0$ . By this means we have introduced explicit energy resolution into a QEP calculation via the integrand in Eq. (7). This approach takes into account a weighting provided by the phonon density of states as a function of phonon energy but the details in the dispersion curves are not explicit, having been integrated over the Brillouin zone. This limits the approach to a detector in the diffraction plane of the microscope that at least covers a Brillouin zone and that should, at the same time, cover a range of scattering angles (q)values) that are small enough to ensure that the relationship between the inelastic signal and the mean squared displacement is still linear to a good approximation.

The inelastic scattering intensity  $I_{\text{inel}}^{\vec{D}}$  in Eq. (7) contains contributions from both energy loss  $\Delta E = +\hbar\omega$  due to excitation as well as possible energy gain  $\Delta E = -\hbar\omega$ due to de-excitation of a single phonon of energy  $E = \hbar \omega$ . To separate the two contributions, we consider Boltzmann factors  $b(E) = \exp(E/k_{\rm B}T)$  expressing the ratio of the probability of vibrational states with quantum numbers n and n+1 being occupied. The factors b(E)/[1+b(E)] and 1/[1+b(E)] can then be used to determine the fractions of energy-loss and energy-gain, respectively. As an example, these factors are plotted in Fig. 3 for a temperature of T = 300 K over the range of phonon energies covered by the PDOS of a silicon crystal. As expected, generally energy loss dominates. However, we note that, for low phonon energies, a substantial amount of intensity is expected on the energy-gain side of the spectrum.

Using the loss and gain fractions, we construct what we term a spectral distribution function (SDF) based on

Eq. (6) as a function of the energy loss  $\Delta E$ , and consistent with Eq. (1) in Ref. [32] and Eq. (3) in Ref. [33], as follows:

$$\begin{split} \text{SDF}(\Delta E) &= C \int g(E) \langle u_{T,E}^2 \rangle \\ &\times \frac{b(E)\delta(E - \Delta E) + \delta(E + \Delta E)}{1 + b(E)} dE \,. \end{split} \tag{8}$$

The first  $\delta$ -function refers to energy loss and the second to energy gain. The constant C is used to normalize the SDF, so that

$$\int SDF(\Delta E) d\Delta E = 1.$$
 (9)

The SDF calculated for silicon at  $T=300~\rm K$  is shown in Fig. 2(b). The spectral distribution function has a different shape when compared to the phonon density of states. Compared to the underlying PDOS, in Fig. 2(a), the contribution from lower phonon energies is enhanced relative to that from higher phonon energies. This is due to the 1/E term and the factor  $\coth(E/2k_{\rm B}T)$  in Eq. (6). A strong peak is expected on the energy-gain side of the SDF originating from de-excitations at phonon energies close to and smaller than the thermal energy  $k_{\rm B}T$ , which is 26 meV at  $T=300~\rm K$ .

### IV. MODELING AND INTERPRETATION OF ENERGY-LOSS SPECTRA

An SDF, calculated for a single atom by the approach discussed in Sec. III, is normalized to unity. To a reasonable approximation, in which we neglect multiple inelastic scattering, the intensity of the energy-loss spectrum due to the phonon scattering of a sample consisting of many atoms and into a detector can be estimated by scaling the SDF using the inelastic scattering signal  $I^D_{\rm inel}$  calculated in the QEP model for the pertinent experimental conditions. The QEP calculation includes effects due to multiple elastic scattering, i.e., channeling effects. While the QEP model provides an appropriate scaling of the spectrum, it doesn't predict a dependence of the shape of the spectrum on probe parameters and on the multiple elastic scattering in the sample. Since the SDF considers single-phonon excitations, this scaling is a better approximation of the intensity for detection geometries, where single-phonon excitations dominate.

Let us now illustrate how the considerations in Sec. III can be applied in the context of modeling and interpreting experimental phonon energy-loss spectra. Venkatraman and co-workers [12] have carried out phonon EELS, recording spectra as a function of probe position for a 60-keV STEM probe with a probe forming aperture having a semi-angle of 28 mrad, on an approximately 500 Å thick silicon crystal oriented down the [110] zone axis. The EELS entrance apertures used were placed on-axis with collection semi angles of 12 and 24 mrad, and we

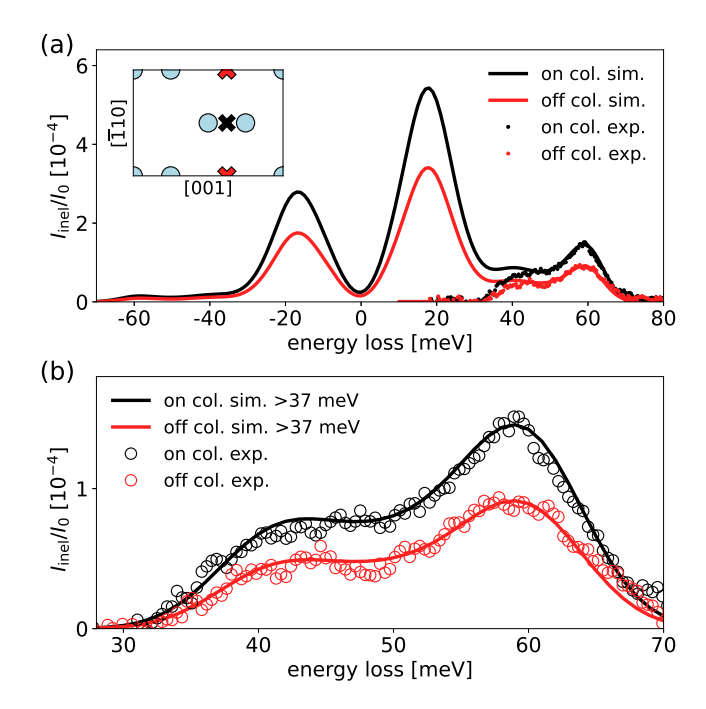


FIG. 4. Simulated phonon EELS for Si [110] at  $T=300~\rm K$ . (a) EELS spectra scaled to fractional inelastic scattering intensity for 500 Å thickness at two probe positions marked by crosses in the inset. Circles in the inset mark atomic positions. Background-subtracted experimental spectra from Ref. [12] are plotted and have been scaled by a common factor (from the given counts). (b) Zoom into the energy-loss range of the experimental data in (a) with the low energy-loss contributions ( $<37~\rm meV$ ) now also removed in the simulation to emulate effects of background correction.

will focus on the latter here. The EELS spectra obtained for this relatively thick specimen are a strong function of the varying channeling conditions encountered when scanning the probe across the specimen.

Consider, for the case of Si in [110] orientation, and with a thickness of 500 Å, the signal contributed to the two different scan points indicated by the crosses in the inset of Fig. 4(a). The spectra plotted in Fig. 4(a) are scaled for the two cases of the probe positioned (i) at the centre of a dumbbell (black curve) and (ii) between dumbbells (red curve). These results were obtained by scaling the pertinent SDF, as calculated according to Eq. (8), to fractional intensity using the intensity  $I_{\text{inel}}$ into a 24 mrad detector calculated in the QEP model for each probe position, see Appendix B for details, relative to the total intensity  $I_0$  of the incident probe. Smoothing was applied to the SDF as shown in Fig. 4 to be consistent with the energy resolution of 9 meV (FWHM), which is slightly lower than what was stated for the experiment [12] but provides a better agreement to the experimental data. The two points correspond to on-column and off-column probe positions for which Venkatraman et al. have measured background subtracted energy-loss spectra (cf. Fig. 2b in Ref. [12]). For comparison with the

calculations, the two experimental spectra from Ref. [12] have been scaled by a common factor from the counts scale to the fractional intensity scale used in the simulations. The simulations reproduce the intensity ratio of the position dependent experimental energy-loss spectra over their whole range.

For a more detailed comparison with the experimental data, Fig. 4(b) is a zoom into the energy-loss range for which the background-subtracted experimental data are available and the curves are now simulated by limiting the contribution to energies in the same energy-loss range. What we can infer is that the background subtraction procedure in Ref. [12], mainly designed to deal with the contributions of the zero-loss peak, has removed most of the phonon sector of the energy-loss spectrum below approximately 30 meV. It will also have removed significant contributions to the spectrum just above 30 meV. In order to emulate the effects of background subtraction in the simulation, we removed contributions by phonon energies below 37 meV. The agreement between theory and experiment is compelling.

The utility of calculating a spectral distribution function by the approach described in Sec. III, using Eq. (8), is further explored by comparison with the experimental data recorded by Li et al. [13] for conditions where the EELS detector is off-axis. Vibrational EELS spectra have been measured across several interfaces in Ref. [13] but we will limit our comparison to the spectra recorded from bulk silicon. We have digitized the EELS spectrum from Fig. S9B of the supplementary material in Ref. [13]. The experiment was performed with 30-keV electrons and with the 25-mrad aperture of the EELS detector effectively tilted away from the optical axis by 80 mrad. This corresponds to a relatively low projected scattering vector of  $q = 1.15 \,\text{Å}^{-1}$ , which is close to the Bragg beams due to the {600} and {440} planes of the silicon crystal. This is the reason for the still quite strong zero-loss peak in the data before background subtraction, part of which is represented by the black dashed curve in Fig. 5. However, the zero-loss peak is greatly reduced compared to the on-axis case and this facilitates a comparison of our simulation with experiment at lower electron energy losses and also on the energy gain side of the spectrum.

Background subtraction was carried out by applying the same model as used by Li et al. [13], i.e., a Pearson type VII function [34]. However, we allow different parameters for the energy-loss and the energy-gain side of the background model, plotted as blue dotted curves in Fig. 5, to handle an asymmetry in the shape of the zero-loss peak [35]. The residual phonon spectrum, obtained by subtracting the background model from the EELS data, is plotted as a green dashed curve for energy losses larger than  $+10~{\rm meV}$  and energy gains below  $-10~{\rm meV}$ .

The SDF was calculated according to Eq. (8), for the given experimental conditions and scaled to counts, as displayed by the red curve in Fig. 5. Besides the devi-

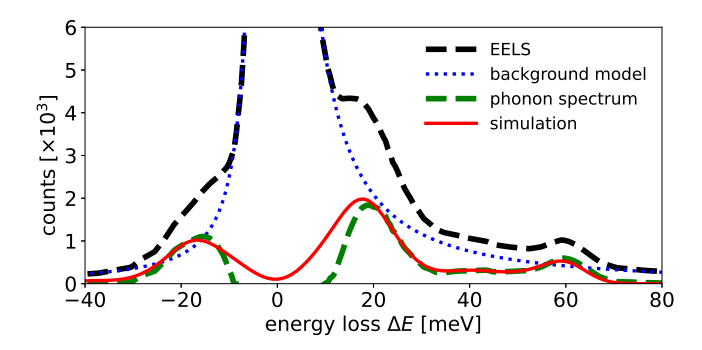


FIG. 5. Off-axis vibrational EELS data as recorded with 30-keV electrons for Si [110] at  $T=300~\mathrm{K}$  by Li et.~al [13] (black dashed) with background model (blue dotted) and residual phonon spectrum (green dashed) in comparison to our simulation (red) for the same conditions. The detector is placed 80 mrad off-axis with a collection semi-angle of 25 mrad.

ations when approaching the strong zero-loss peak, the simulation is in good agreement to the experiment, considering that somewhat larger scattering angles are involved for the off-axis detector. In particular, the relative heights of the main peaks are well reproduced. It should be noted though that the peak ratios of the residual phonon spectrum are sensitive to background modeling.

#### V. SUMMARY AND DISCUSSION

We have introduced a simple, albeit approximate, approach to simulating spectra in the phonon sector in STEM EELS. A normalized spectral distribution function is derived from the PDOS, assuming proportionality of inelastic scattering to the mean-squared atomic displacements as a function of phonon energy. Boltzmann factors are applied to estimate the contributions of energy loss and gain in the spectrum. The spectral distribution function is then used to distribute the total inelastic scattering intensity as a function of the position of the STEM probe obtained by a QEP model calculation that uses an average MSD at a temperature that is derived from the same PDOS. This approach is valid for single-phonon excitation and has been shown to give good agreement with experimental data recorded with high-energy resolution EELS for a detector covering at least the first Brillouin zone and that, at the same time, covers a range of scattering angles that ensures dominance of single-phonon excitations. Multi-phonon excitations, which are expected to be more important at larger scattering angles, contribute approximately uniformly across the EELS spectrum. This means that they are likely to contribute to a smooth background which will largely be removed from experimental data during background subtraction.

The effect of multiple elastic scattering on the total amount of inelastic scattering for different probe position or thickness is incorporated via a QEP calculation.

However, a spectrum derived by scaling a spectral distribution function with the QEP result is in a single inelastic scattering approximation, implying that this is a valid approach for thinner specimens, where single inelastic scattering dominates. Differences in the shape of the spectrum as a function of sample thickness, i.e., a different thickness dependence for different phonon energies [24, 26], is not a feature of the proposed approach. Also, changes in the shape of the spectrum as a function of a STEM probe used is not accounted for.

Although peaks in the input phonon density of states generally correspond to those in the calculated electron energy-loss spectra, the spectra differ significantly from the phonon density of states. In particular, contributions from low phonon energies are enhanced compared to those from high phonon energies. The effect of temperature is taken into account and it has an influence on the shape of the spectrum, mostly on how strong the fractions of energy-gain and energy-loss are. The scaling of an energy-loss/gain spectrum with optical parameters, often varied in QEP calculations in STEM, such as electron wavelength, probe convergence angle, zone axis orientation, mistilt with respect to a zone axis, or partial coherence can easily be investigated using the model proposed.

An essential aspect of the approach to vibrational EELS presented here is that it connects the phonon density of states to a measured spectrum in an approximate way. Here we have demonstrated how to calculate a spectrum from a density of states. However, going from a measured spectrum to a density of states is likewise possible, and these may be spectra measured locally as a function of STEM probe position. Effectively, this can be achieved by taking the loss side of a spectrum  $s(\Delta E)$ , which can be considered as an unnormalized version of the SDF for a subset of the energy-loss range (due to background correction). We then substitute energy loss  $\Delta E$  with phonon energy E, assuming dominance of single-phonon excitations, and apply an inversion of Eq. (8) in the form

$$g(E) \propto E \frac{1 + b(E)}{b(E)} \tanh\left(\frac{E}{2k_{\rm B}T}\right) s(E)$$
$$= E \left[1 - \exp\left(-\frac{E}{k_{\rm B}T}\right)\right] s(E). \tag{10}$$

In the final line the fractional occupation factors involving the function  $b(E) = \exp(E/k_{\rm B}T)$  have been combined with the tanh-function and constants have been omitted in expressing a proportionality of the result to the phonon density of states. It is also possible to reconstruct g(E) from the gain side of a spectrum in an analogous way. A local PDOS obtained in this way can be compared to one projected on a given atom or a subset of atoms in first-principles calculations. Likewise, a PDOS projected to a local subset of atoms could be used to calculate a local energy-loss/gain spectrum, assuming perfect localization of the inelastic scattering. The assumption of a local response would not be justified for

vibrational EELS of ionic compounds measured on-axis, but would hold for off-axis detection [21]. Any possible effect of multiple scattering on the shape of the spectrum would not be included in such a simple approach.

Anisotropy of a crystal can be included in this approach, in as much as it is included in the applied effective PDOS. For example, for a particular crystal orientation, the components of the vibrational modes that are perpendicular to the incident beam direction dominate in the spectrum. This means, an effective PDOS applies in general, a subtlety which has been ignored here. One can also describe compounds with multiple atom types, where a specific partial PDOS is available and projected on each atom in a unit cell. Preserving the relative ratio of each partial PDOS to the total PDOS, a partial SDF can be computed for each atom type, and the total SDF is then obtained by normalizing the sum of the partial distribution functions. Respective contributions of each atom type to the total SDF could be separated.

#### ACKNOWLEDGMENTS

We acknowledge the support of the Swedish Research Council, Olle Engkvist's foundation, Carl Trygger's Foundation, Knut and Alice Wallenberg Foundation for financial support. Simulations were enabled by resources provided by the Swedish National Infrastructure for Computing (SNIC) at NSC Centre partially funded by the Swedish Research Council through Grant Agreement No. 2018-05973.

## Appendix A: Components of scattering in the QEP model

In the QEP model [18] we generate a set  $\{\phi_j\}$  of N so-called auxiliary functions. An auxiliary function  $\phi_j$  is obtained by propagating the probe through the specimen to the exit surface for a positional configuration of the atoms, and positional configurations are usually calculated in an Einstein model using a Gaussian probability distribution function for atomic displacements. The total intensity observed in the diffraction plane is given by the incoherent average

$$I(\mathbf{q}) = \frac{1}{N} \sum_{j} |\phi_j(\mathbf{q})|^2 , \qquad (A1)$$

where  $\phi_j(\mathbf{q})$  is the Fourier transform to the diffraction plane of the auxiliary function j. The elastic contribution to the diffraction pattern is given by taking the modulus squared of the coherent sum

$$\phi_{\text{elas}}(\mathbf{q}) = \frac{1}{N} \sum_{j} \phi_{j}(\mathbf{q}) .$$
 (A2)

From these two quantities, the intensity due to inelastic scattering is calculated by

$$I_{\text{inel}}(\mathbf{q}) = I(\mathbf{q}) - |\phi_{\text{elas}}(\mathbf{q})|^2.$$
 (A3)

The inelastic intensity  $I_{\text{inel}}^D$  recorded by a detector placed in the diffraction plane is calculated by integrating  $I_{\text{inel}}(\mathbf{q})$  over the appropriate range of  $\mathbf{q}$  vectors.

## Appendix B: QEP model simulations for Si

The QEP calculations have been carried out with the freely available and open source program  $\mu$ STEM [36] using a version compiled in double precision. The structure model for crystalline Si was taken from Ref. [37] and an isotropic thermal vibration parameter of  $\langle u_T^2 \rangle = 0.00587 \text{ Å}^2$  was used. In the case of Si, the crystal was aligned with the [110] axis along the incident probe direction, with perpendicular orientations as shown in the inset in Fig. 4(a). Positional configurations for the QEP-

type calculations were generated for a supercell of size of a = 27.1525 Å, b = 26.8800 Å and c = 3.8403 Å, whichcontains the projected Si [110] unit in a tiling of  $5 \times 7$ along the a and b axes, respectively. The scattering potentials were constructed using the tables of Waasmaier and Kirfel [38] and sampled on a grid of  $512 \times 512$  pixels for the a and b supercell dimensions and using two slices along the c direction (one for each atomic plane). For each slice, 400 positional configurations were calculated and stacked randomly up to a thickness of 500 Å for each QEP pass. In order to simulate STEM imaging and phonon EELS mapping in comparison to the experimental data of Venkatraman et al. [12] an incident electron probe of 60 keV kinetic energy and 28-mrad convergence semi-angle was scanned over  $13 \times 9$  probe positions, evenly distributed across the projected Si [110] unit cell, and with 400 QEP passes per probe position. Spatial coherence was taken into account by convolution of the scans with an effective Gaussian source distribution of 1.5 Å full width at half maximum.

- [1] O. L. Krivanek, T. C. Lovejoy, N. Dellby, T. Aoki, R. W. Carpenter, P. Rez, E. Soignard, J. Zhu, P. E. Batson, M. J. Lagos, R. F. Egerton, and P. A. Crozier, Vibrational spectroscopy in the electron microscope, Nature (London) 514, 209 (2014).
- [2] C. Dwyer, T. Aoki, P. Rez, S. L. Y. Chang, T. C. Lovejoy, and O. L. Krivanek, Electron-beam mapping of vibrational modes with nanometer spatial resolution, Phys. Rev. Lett. 117, 256101 (2016).
- [3] M. J. Lagos, A. Trügler, U. Hohenester, and P. E. Batson, Mapping vibrational surface and bulk modes in a single nanocube, Nature (London) 543, 529 (2017).
- [4] M. J. Lagos and P. E. Batson, Thermometry with subnanometer resolution in the electron microscope using the principle of detailed balancing, Nano Lett. 18, 4556 (2018).
- [5] J. A. Hachtel, J. Huang, I. Popovs, S. Jansone-Popova, J. K. Keum, J. Jakowski, T. C. Lovejoy, N. Dellby, O. L. Krivanek, and J. C. Idrobo, Identification of site-specific isotopic labels by vibrational spectroscopy in the electron microscope, Science 363, 525 (2019).
- [6] F. S. Hage, D. M. Kepaptsoglou, Q. M. Ramasse, and L. J. Allen, Phonon spectroscopy at atomic resolution, Phys. Rev. Lett. 122, 016103 (2019).
- [7] G. Radtke, D. Taverna, N. Menguy, S. Pandolfi, A. Courac, Y. Le Godec, O. Krivanek, and T. Lovejoy, Polarization selectivity in vibrational electron-energyloss spectroscopy, Phys. Rev. Lett. 123, 256001 (2019).
- [8] R. Senga, K. Suenaga, P. Barone, S. Morishita, F. Mauri, and T. Pichler, Position and momentum mapping of vibrations in graphene nanostructures, Nature (London) 573, 247 (2019).
- [9] S. M. Collins, D. M. Kepaptsoglou, J. Hou, C. W. Ashling, G. Radtke, T. D. Bennett, P. A. Midgley, and Q. M. Ramasse, Functional group mapping by electron beam vibrational spectroscopy from nanoscale volumes, Nano

- Lett. 20, 1272 (2020).
- [10] F. S. Hage, G. Radtke, D. M. Kepaptsoglou, M. Lazzeri, and Q. M. Ramasse, Single-atom vibrational spectroscopy in the scanning transmission electron microscope, Science 367, 1124 (2020).
- [11] X. Yan, C. Liu, C. A. Gadre, L. Gu, T. Aoki, T. C. Lovejoy, N. Dellby, O. L. Krivanek, D. G. Schlom, R. Wu, and X. Pan, Single-defect phonons imaged by electron microscopy, Nature (London) 589, 65 (2021).
- [12] K. Venkatraman, B. D. Levin, K. March, P. Rez, and P. A. Crozier, Vibrational spectroscopy at atomic resolution with electron impact scattering, Nat. Phys. 15, 1237 (2019).
- [13] Y.-H. Li, R.-S. Qi, R.-C. Shi, J.-N. Hu, Z.-T. Liu, Y.-W. Sun, M.-Q. Li, N. Li, C.-L. Song, L. Wang, Z.-B. Hao, Y. Luo, Q.-K. Xue, X.-C. Ma, and P. Gao, Atomic-scale probing of heterointerface phonon bridges in nitride semiconductor, Proceedings of the National Academy of Sciences 119, e2117027119 (2022).
- [14] T. Lee, J. Qi, C. A. Gadre, H. Huyan, S.-T. Ko, Y. Zuo, C. Du, J. Li, T. Aoki, R. Wu, et al., Atomic-scale origin of the low grain-boundary resistance in perovskite solid electrolyte Li<sub>0.375</sub>Sr<sub>0.4375</sub>Ta<sub>0.75</sub>Zr<sub>0.25</sub>O<sub>3</sub>, Nature Communications 14, 1940 (2023).
- [15] L. J. Allen and T. W. Josefsson, Inelastic scattering of fast electrons by crystals, Phys. Rev. B 52, 3184 (1995).
- [16] A. Amali and P. Rez, Theory of lattice resolution in highangle annular dark-field images, Microscopy and Microanalysis 3, 28 (1997).
- [17] A. V. Martin, S. D. Findlay, and L. J. Allen, Model of phonon excitation by fast electrons in a crystal with correlated atomic motion, Phys. Rev. B 80, 024308 (2009).
- [18] B. D. Forbes, A. V. Martin, S. D. Findlay, A. J. D'Alfonso, and L. J. Allen, Quantum mechanical model for phonon excitation in electron diffraction and imaging using a Born-Oppenheimer approximation, Phys. Rev. B

- **82**, 104103 (2010).
- [19] N. R. Lugg, B. D. Forbes, S. D. Findlay, and L. J. Allen, Atomic resolution imaging using electron energy-loss phonon spectroscopy, Phys. Rev. B 91, 144108 (2015).
- [20] B. D. Forbes and L. J. Allen, Modeling energy-loss spectra due to phonon excitation, Phys. Rev. B 94, 014110 (2016).
- [21] C. Dwyer, Prospects of spatial resolution in vibrational electron energy loss spectroscopy: Implications of dipolar scattering, Phys. Rev. B 96, 224102 (2017).
- [22] L. J. Allen, H. G. Brown, S. D. Findlay, and B. D. Forbes, A quantum mechanical exploration of phonon energy-loss spectroscopy using electrons in the aloof beam geometry, Microscopy 67, i24 (2018).
- [23] R. J. Nicholls, F. S. Hage, D. G. McCulloch, Q. M. Ramasse, K. Refson, and J. R. Yates, Theory of momentum-resolved phonon spectroscopy in the electron microscope, Phys. Rev. B 99, 094105 (2019).
- [24] P. Rez and A. Singh, Lattice resolution of vibrational modes in the electron microscope, Ultramicroscopy 220, 113162 (2021).
- [25] P. M. Zeiger and J. Rusz, Efficient and versatile model for vibrational STEM-EELS, Phys. Rev. Lett. 124, 025501 (2020).
- [26] P. M. Zeiger and J. Rusz, Frequency-resolved frozen phonon multislice method and its application to vibrational electron energy loss spectroscopy using parallel illumination, Phys. Rev. B 104, 104301 (2021).
- [27] P. Zeiger, J. Barthel, L. J. Allen, and J. Rusz, Lessons from the harmonic oscillator – a reconciliation of the frequency-resolved frozen phonon multislice method with other theoretical approaches, Phys. Rev. B , in press (2023).
- [28] P. Brüesch, Phonons: Theory and Experiments II: Experiments and Interpretation of Experimental Results,

- Vol. 65 (Springer-Verlag, Berlin, 1986).
- [29] H. Gao and L.-M. Peng, Parameterization of the temperature dependence of the Debye-Waller factors, Acta Crystallogr. Sect. A 55, 926 (1999).
- [30] D. Kim, H. L. Smith, J. L. Niedziela, C. W. Li, D. L. Abernathy, and B. Fultz, Phonon anharmonicity in silicon from 100 to 1500 k, Phys. Rev. B 91, 014307 (2015).
- [31] N. Butt, J. Bashir, B. Willis, and G. Heger, Compilation of temperature factors of cubic elements, Acta Crystallogr. Sect. A 44, 396 (1988).
- [32] R. E. DeWames and W. F. Hall, A relation between the energy loss spectrum of incoherently scattered electrons and the phonon density of states in crystals, physica status solidi (b) **20**, K11 (1967).
- [33] P. Batson and M. Lagos, Interpretation of mev resolution phonon eels data, Microscopy and Microanalysis 24, 412–413 (2018).
- [34] K. Pearson, IX. mathematical contributions to the theory of evolution.—XIX. Second supplement to a memoir on skew variation, Philosophical Transactions of the Royal Society of London. Series A, Containing Papers of a Mathematical or Physical Character 216, 429 (1916).
- [35] J. A. Hachtel, A. R. Lupini, and J. C. Idrobo, Exploring the capabilities of monochromated electron energy loss spectroscopy in the infrared regime, Scientific Reports 8, 5637 (2018).
- [36] L. J. Allen, A. J. D'Alfonso, and S. D. Findlay, Modelling the inelastic scattering of fast electrons, Ultramicroscopy 151, 11 (2015).
- [37] D. N. Batchelder and R. O. Simmons, Lattice constants and thermal expansivities of silicon and of calcium fluoride between 6° and 322°K, J. Chem. Phys. 41, 2324 (1964).
- [38] D. Waasmaier and A. Kirfel, New analytical scatteringfactor functions for free atoms and ions, Acta Crystallogr. Sect. A 51, 416 (1995).